Applied Physics Letters

Two-photon electromagnetic induction imaging with an atomic magnetometer

Cite as: Appl. Phys. Lett. **122**, 144001 (2023); https://doi.org/10.1063/5.0147291
Submitted: 21 February 2023 • Accepted: 19 March 2023 • Published Online: 04 April 2023

Benjamin Maddox and Ferruccio Renzoni

Applied Physics Letters ARTICLE scitation.org/journal/apl

Two-photon electromagnetic induction imaging with an atomic magnetometer

Cite as: Appl. Phys. Lett. **122**, 144001 (2023); doi: 10.1063/5.0147291
Submitted: 21 February 2023 · Accepted: 19 March 2023 ·
Published Online: 4 April 2023

View Online Export Citation CrossMark

Benjamin Maddox and Ferruccio Renzoni[a)]

AFFILIATIONS

Department of Physics and Astronomy, University College London, Gower Street, London WC1E 6BT, United Kingdom

[a)]Author to whom correspondence should be addressed: f.renzoni@ucl.ac.uk

ABSTRACT

Electromagnetic induction imaging (EMI) is a contactless, nondestructive evaluation technique based on sensing the response of a target to oscillating magnetic fields as they penetrate into materials. Leveraging the enhanced performance of radio frequency atomic magnetometers (RF-AMs) at low frequencies can enable highly sensitive through-barrier EMI measurements, which, for example, can reveal concealed weaponry or inspect subsurface material defects. However, deriving this advantage requires precise control of a well-defined, low bias magnetic field with respect to the background magnetic field texture, which presents a cumbersome challenge to stabilize in real-world unshielded scenarios. Here, we implement a two-photon RF-AM scheme in a portable setup to bypass the requirement of a low bias field and achieve stable, repeatable resonances in the sub-kHz regime. The improved accessibility to lower primary field frequencies offer greater skin-depth in target materials and facilitates an enhancement of a factor of 8 in skin penetration with this portable system, detecting features behind an Al shield of 3.2 mm. The scheme also reduces the need of large compensation coils to stabilize the bias field, facilitating the implementation of compact devices.

Electromagnetic induction imaging (EMI) enables nondestructive and noninvasive tomographic conductivity imaging of targets over a wide range of conductivities.[1] Exciting a target with a primary oscillating magnetic field produces eddy currents in the material, which, in turn, generate secondary oscillating fields that can be sensed with a probing magnetometer. The skin-effect constrains the maximum penetration achievable by the primary field, therefore enabling a tomographic image to be formed by varying the primary frequency. Pushing the technique to super-mm penetration depths in conductive targets requires frequencies in the sub-kHz regime, a requirement that makes the choice of the sensor critical for EMI performance. While the signal-to-noise ratio (SNR) of the induction coil weakens with lower frequencies, the fundamental sensitivity of radio frequency atomic magnetometers (RF-AMs) remains flat and presents the opportunity to gain over three orders of magnitude advantage in RF sensitivity at 1 kHz.[2] Interest in exploiting this advantage has been increasing, with multiple groups now advancing this technique.[3–8] This enhancement comes at the cost of robustness, as RF-AMs demand a well-defined static magnetic field, typically called the bias field, to produce a stable resonance. To produce a resonance in the sub-kHz regime requires $B_{\mathrm{Bias}} < 1.43$ mG, which becomes comparable to the order of the earth's magnetic field temporal/spatial fluctuations. Conventionally, this problem is circumvented by attenuating the background field with magnetic shielding, but many applications require RF-AMs to work in real-world environments where shielding is impossible to achieve or unwanted. Active magnetic field cancellation has proved effective at stabilizing the bias field in many applications in real-world environments.[9–11] However, this method fights a losing battle to the background field as low-frequency operation requires a reduced bias field, which increases the influence of transverse field noise and gradient noise, with resulting decrease in sensitivity.[12] To combat this, in this work, we drive the RF-AM with a two-photon RF transition.[13] As in the proposed system, the required bias field strength is determined by the sum of the frequency of the two photons, for a convenient choice of very unequal frequencies of the two photons it is possible to operate the magnetometer at ultra-low frequency while maintaining a large enough bias field to guarantee stable operation and high sensitivity in an unshielded environment. The approach affords us the stability to perform ultra-low frequency EMI, and as a result, achieve deeper through-barrier penetration.

The requirement of low-frequency operation of EMI systems to achieve penetration through a barrier, as required in security and

surveillance applications, derives from the dependence of the penetration depth of an oscillating magnetic field through a material on the field frequency. An oscillating magnetic field decays evanescently through a target material depth z according to Ref. 14,

$$B_{RF}(z) = B_{RF}(0)e^{-z/\delta(\omega_{RF})}, \tag{1}$$

where δ represents the skin depth, which at low frequencies becomes

$$\delta(\omega_{RF}) = \sqrt{\frac{2}{\omega_{RF}\sigma\mu}}, \tag{2}$$

where μ, ε, and σ are the magnetic permeability, electrical permittivity, and the electrical conductivity of the target material, respectively. Equation (2) shows the nonlinear payoff in penetration depth by reducing the primary field frequency and illustrates the requirement of low-frequency operation for penetration through barriers.

Figure 1(a) illustrates the working principle in the conventional RF-AM: a vapor of ^{87}Rb is illuminated by a circularly polarized pump beam propagating parallel to a bias magnetic field B_{Bias} in the $\hat{x}$ direction, transferring most of the atomic population into the stretched state of the upper hyperfine groundstate. An RF field B_{RF}, perpendicular to B_{Bias} and resonant with the Zeeman splitting of the magnetic sublevels, creates an oscillating population transfer in the hyperfine manifold. This then manifests as an oscillating refractive index to a detuned probe beam propagating perpendicularly to B_{Bias} and appears as an oscillating polarization rotation when read-off by a polarimeter. B_{Bias} generates the groundstate magnetic sublevel splitting via the Zeeman effect and sets the resonant frequency ω_0 as

$$\omega_0 = \gamma B_{\text{Bias}}, \tag{3}$$

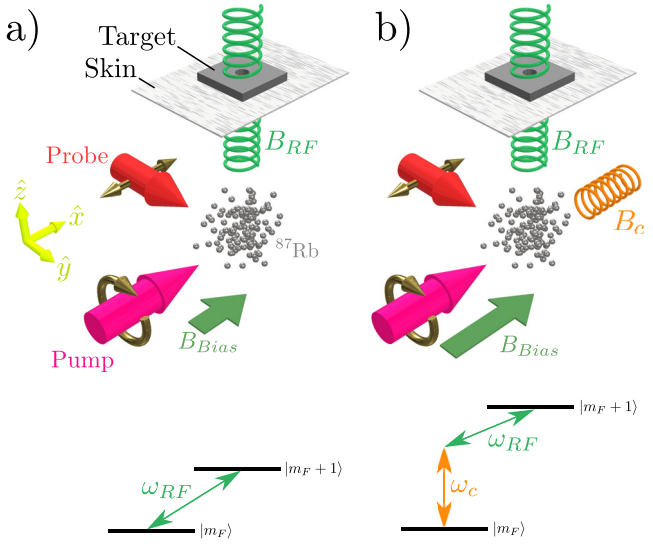

FIG. 1. Geometry of the one-photon (a) and two-photon (b) setup along with a reduced level diagram showing adjacent magnetic sublevels in the groundstate and the coupling mechanism in each case. The magenta and red arrows show the pump and probe beam direction as they traverse through the atomic medium (silver spheres), while the copper arrows indicate the light polarization.

where γ is the gyromagnetic ratio of the valence electron of the probed atom. Since B_{Bias} and any spurious transverse magnetic field $B_\perp$ sum in quadrature[12]

$$\delta B_{TOT} = \frac{\delta B_\perp^2}{B_{\text{Bias}}}, \tag{4}$$

where we assumed $B_\perp \simeq \delta B_\perp$ as no static field is applied in the transverse direction, the noise on the total field seen by the atoms B_{TOT} becomes more and more dominated by transverse field noise as B_{Bias} reduces. Further complications arise when considering the direction of B_{TOT} with respect to the pump beam propagation. As transverse field noise increase, so too does the angular noise, which the atoms experience as a polarization noise on the pump beam, diminishing the atomic polarization, which translates to amplitude noise. Active compensation can accommodate for the zeroth- and first-order magnetic field gradients

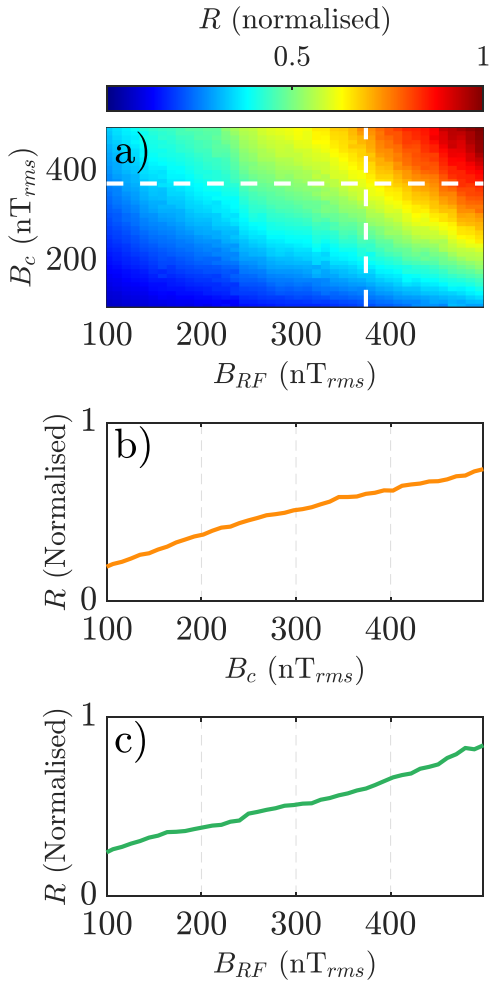

FIG. 2. Surface (a) of the two-photon RF-AM amplitude as a function of B_{RF} and B_c along with cross sections (b) and (c) of the individual parameters. Here, $\omega_{RF} = 2\pi \times 3$ kHz, $\omega_c = 2\pi \times 47$ kHz, and the bias field was set to produce a resonance at $\omega_0 = 2\pi \times 50$ kHz. White dashed lines in (a) show the positions of the cross sections for (b) and (c).

with Helmholtz and anti-Helmholtz coils, respectively, but the nonlinear texture of the background prevails and is challenging to deal with.

In the two-photon scheme shown in Fig. 1(b), two RF photons with different polarizations are used. The scheme relies on the fact that π-polarized RF photons drive $\Delta m = 0$ transitions and $\sigma^{\pm}$ photons drive $\Delta m = \pm 1$ transitions. In the proposed scheme, an additional RF field B_c, propagating along B_{Bias}, facilitates a two-photon transition at $\omega_{RF} = \omega_0 - \omega_c$. When added to the σ polarized B_{RF} photon, the π polarization of the B_c photon allows the selection rule of $\Delta m = \pm 1$ to be satisfied and, therefore, couple adjacent magnetic sublevels. Tuning ω_c effectively shifts the RF-AM resonance with respect to ω_{RF}, without the need to alter B_{Bias}. The Rabi frequency of the two-photon transition is given by Geng *et al.*,[13]

$$\Omega = \frac{\Omega_{RF}\Omega_c}{4\omega_c}, \tag{5}$$

which allows the same linearity in Ω_{RF} as is the case for the standard RF-AM configuration except with an additional factor of $\Omega_c/4\omega_c$. EMI measurements are generally based on the ratio of the primary B_{RF} and secondary field δB_{RF},[1]

$$\frac{\delta B_{RF}}{B_{RF}} \propto \omega_{RF}(\omega_{RF}\varepsilon_0\varepsilon_r - i\sigma), \tag{6}$$

and since $\Omega_{RF} \propto B_{RF}$, we require only the linearity of the two-photon RF-AM amplitude on Ω_{RF} for EMI measurements.

The portable RF-AM setup has been described in detail previously.[15] Briefly, an isotopically enriched ^{87}Rb vapor cell and the optical and magnetic systems required for an RF-AM are enclosed within a nylon sensor head of dimensions $110 \times 110 \times 145\ \text{mm}^3$ (W × L × H) and of weight 1.49 kg. To reduce wall relaxation and increase atomic interaction time, the cubic vapor cell (25 mm side length) is filled with 20 Torr of N_2 as a buffer gas and held at room temperature. Laser light for pump and probe beams is provided by two VCSEL (vertical-cavity surface-emitting laser) diodes, expanded by lenses to diameters of 10 mm. B_{Bias} is generated and stabilized by active magnetic stabilization via three pairs of orthogonally orientated square Helmholtz coils, centered on the vapor cell. An additional anti-Helmholtz coil is aligned along $\hat{x}$ to compensate for linear gradients in the bias field. Internal fluxgate sensors are used to measure the DC magnetic fields (bandwidth 100 Hz) in all three axes and are fed to proportional-integral-derivative (PID) controllers to adjust the compensation coil currents. Internal RF coils provide B_{RF} and B_c. An external lock-in amplifier (LIA) demodulates the polarimeter at $\omega/2\pi$ and outputs the amplitude R of the magnetic resonance. The resonance is swept with the RF fields and a linewidth (HWHM) of the resonance $\Gamma = 2\pi \times 680$ Hz is typical for the system. The portable RF-AM is raster-scanned across an object using a 2D mechanical translational stage and builds up a conductivity image of static targets, which has been able to detect features masked by conductive shields[16] and simulated corrosion under insulation.[17]

For the two-photon scheme, two identical RF coils (6 mm diameter and 10 mm length) are driven by waveform generators, at their respective frequencies of ω_{RF} and ω_c. The B_{RF} coil is positioned under the target 50 mm above the vapor cell in the z axis, while the B_c RF coil is aligned along the x axis and also displaced by 50 mm. The

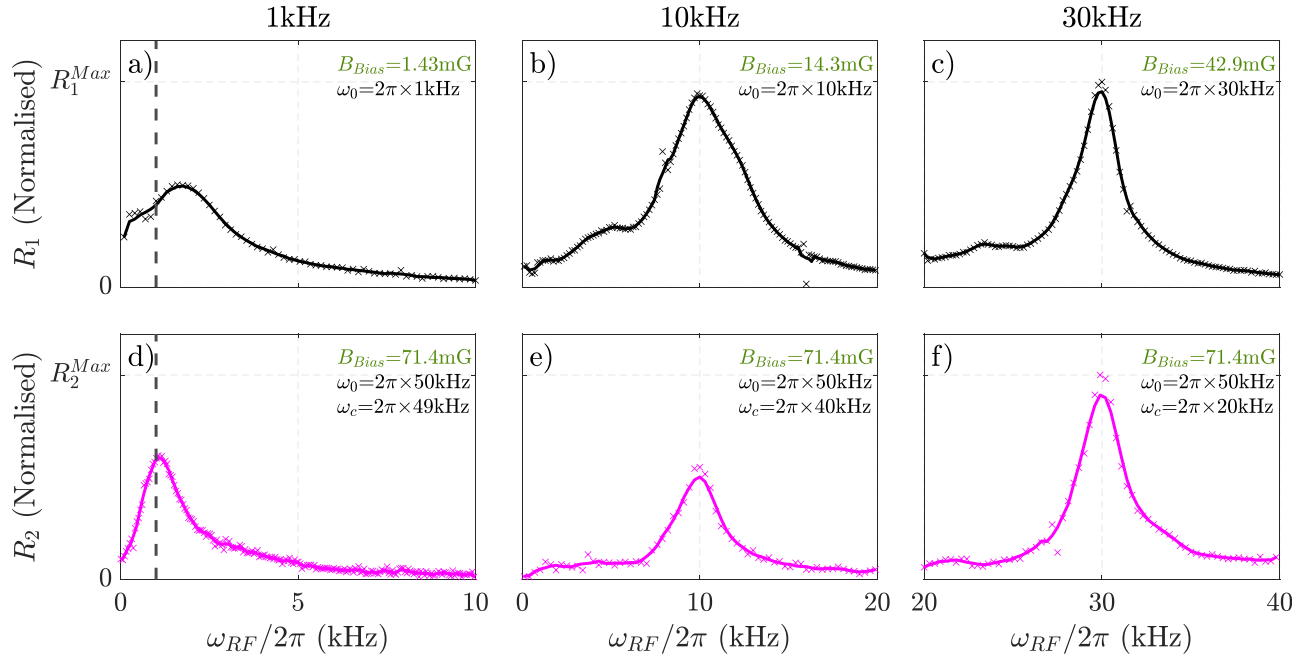

FIG. 3. Magnetic resonances for the one-photon (a)–(c) and two-photon scheme (d-f) as the desired resonant primary field frequency ω_{RF} is lowered. Column titles show the nominal $\omega_{RF}/2\pi$ that is desired from the system. The LIA output $R_{1,2}$ for the one- and two-photon case, respectively, is normalized to the peak measured value at the largest ω_{RF} considered. For the one-photon scheme, the bias field is reduced to set ω_0 at the desired ω_{RF}, whereas for the two-photon scheme, ω_0 is fixed and the coupling field ω_c is set such that $\omega_0 - \omega_c$ gives the desired ω_{RF}. Crosses show the raw data while lines show smoothed averages of the data to guide the eyes. The vertical black dashed line in (a) and (d) represents $\omega_{RF}/2\pi = 1$ kHz.

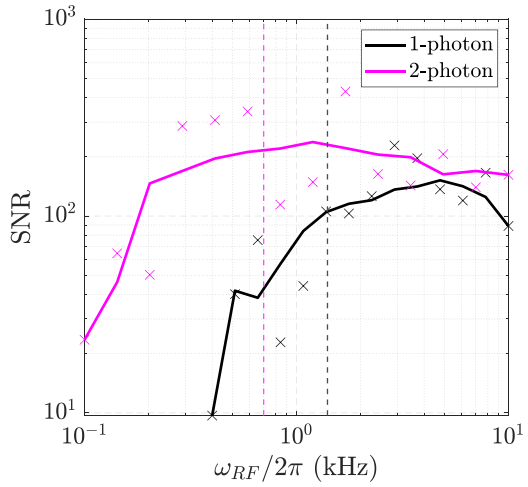

FIG. 4. SNR of the two schemes when matched in Rabi frequency. Crosses show raw data points while lines show a smoothed average to guide the eyes. The black vertical dashed line shows the minimum achievable one-photon resonant frequency of $\omega_0/2\pi = 1.6$ kHz, while the dashed magenta line shows the linewidth $\Gamma/2\pi = 680$ Hz.

polarimeter signal is then demodulated at ω_0 by a lock-in amplifier via an internal reference set at ω_0. Figure 2(a) shows a surface of the two-photon RF-AM amplitude as a function of B_{RF} and B_c, with cross sections in Fig. 2(b) and 2(c). We, thus, verified the linearity of the amplitude of the RF-AM on B_{RF}, as predicted by Eq. (5). Such a linearity is required for the two-photon EMI approach introduced in this work.

Figure 3 demonstrates the tunability of the two-photon RF-AM configuration compared to the standard one-photon configuration. For the standard configuration, the bias field is reduced to give the resonance at lower frequencies; however, it becomes impossible to attain a resonance at $\omega_{RF}/2\pi = 1$ kHz despite transverse nulling and linear gradient compensation coils, with the minimum achievable resonance being $\omega_0/2\pi = 1.6$ kHz. It is at this point that the bias field is comparable with the background and the field over the cell is dominated by the texture of the background field and since the RF-AM measurement will be an average of the bias field felt by all the atoms in the pump-probe intersection volume, some non-zero field appears due to nonlinear background gradients. The two-photon configuration has no such limitation, and it easily fulfills the condition of $\omega_{RF}/2\pi = 1$ kHz just by adjusting ω_c. The simplicity in tuning the two-photon resonance effectively bypasses the need to adjust transverse field/gradient field setpoints that would normally be required in bias field tuning.[18]

Reinforcing this is an analysis of the SNR of the two configurations in Fig. 4. With their Rabi coupling matched between the two schemes, both are swept to low frequencies and the SNR is calculated from fast Fourier transform (FFT) traces with B_{RF} on and off at each frequency. Again for the one-photon case, the bias field is adjusted to get maximum signal at each point, whereas for two-photon case, ω_0 stays static and ω_c is adjusted. At high frequencies, the SNR is comparable between the two schemes, but as the frequency is lowered below the minimum resonance set by the bias field stabilization $\omega_0/2\pi = 1.6$ kHz (black dashed line) the SNR drops by an order of magnitude. The two-photon case, however, maintains the SNR through the sub-kHz regime until dropping below 300 Hz. The ultimate decline of the two-photon case is due to ω_{RF} approaching the linewidth Γ of the magnetic resonance, which puts ω_c in the vicinity of the standard one-photon resonance. Despite the RF coil that produces B_c being aligned

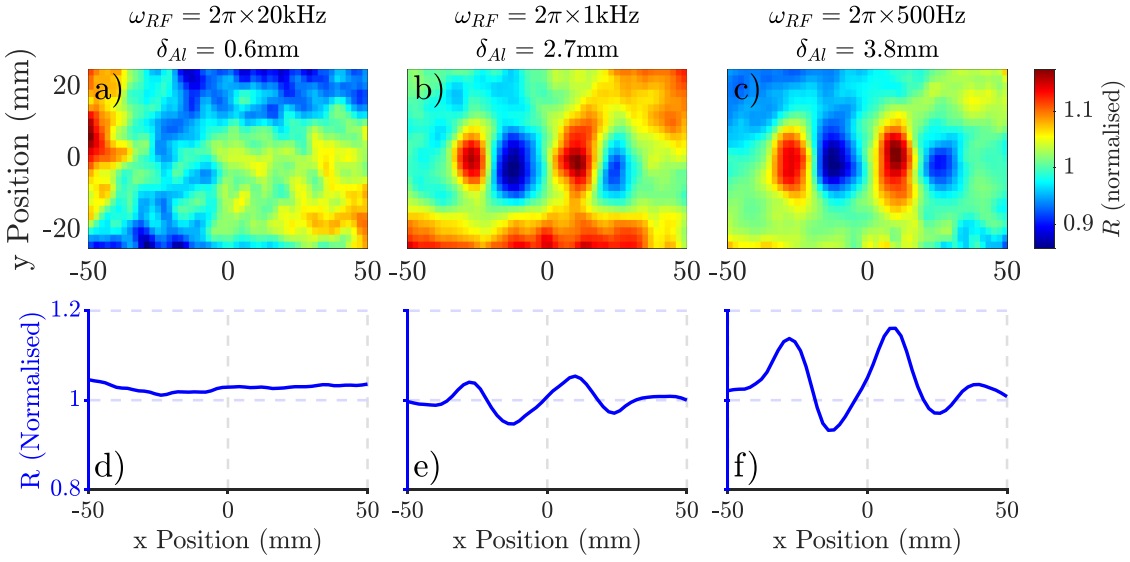

FIG. 5. Two-photon EMI of the double-hole target concealed by 2 mm thick Al skin, at three different values of $\omega_{RF}/2\pi$: (a) 20 kHz, (b) 1 kHz, and (c) 500 Hz along with respective averages through the horizontal axis in (d)–(f). The bias field is set to give a resonance at $\omega_0/2\pi = 53$ kHz and ω_c is swept at each pixel to fulfill the two-photon resonance condition. Amplitudes for each image are normalized to the corner pixel such that contrast can be compared between the panels. For each pixel, the portable RF-AM is moved by a 2 mm step in the *x*–*y* plane and a Gaussian filter with a width of 1 pixel is used to smooth the image.

along the RF-AM deadzone, which should attenuate any one-photon driving by the coupling field,[19] the RF coil will have some small transverse components, which will couple and inevitably begin to competitively interfere with the two-photon process when on resonance.

Figure 5 shows a demonstration of through-barrier EMI imaging with the two-photon RF-AM. An Al sheet of thickness $d_{\text{skin}} = 2$ mm conceals a block of Al with two 16 mm diameter holes spaced 36.7 mm apart. The RF-AM is aligned underneath (see Fig. 1) at a standoff of ~0.5 mm. For each pixel, the portable RF-AM is mechanically actuated in the x–y plane, ω_{RF} is held fixed and ω_c is swept through the two-photon resonance to determine the maximum amplitude. For imaging, we desire only the effect of B_{RF} on the target material, and therefore, it is important to note the geometry of the two RF coils. The B_c coil is not only separated from the target by much larger distance than the B_{RF} coil (greater than 100 times the standoff) but it is also orthogonally aligned to the surface, which is enough to neglect any contribution from the coupling field in the EMI measurements. At 20 kHz, B_{RF} fails to penetrate the shielding as $\delta_{\text{Al}} < d_{\text{skin}}$. When $\delta_{\text{Al}} \approx d_{\text{skin}}$ the structure of the holes through the skin appears, which matches our expectation from previous studies.[16,20–22] Due to eddy current excitation on the plane inside the hole, a portion of the secondary field becomes spatially transverse to the primary field and leads to a dispersive-like shape on the amplitude of the RF-AM. As $\delta_{Al} > d_{\text{skin}}$, the structure becomes clearer and confirms that the two-photon RF-AM can perform feasible EMI measurements. Finally, in Fig. 6, we show the thickest Al skin that can be imaged with two-photon EMI for this particular setup. The features of the double-hole target are clearly revealed from behind an Al skin of 3.2 mm thickness, which improves upon our previous study with this system[16] by a factor of 8.

We have demonstrated the effectiveness of a two-photon excitation scheme in RF-AMs for increasing the efficacy of through-barrier EMI detection of holes in Al that are obscured by super-mm thick Al skins. The technique effectively removes the bottleneck of extremely precise and homogeneous magnetic field compensation in unshielded environments, which sets limits on miniaturization and presents a demanding engineering challenge. Furthermore, looking at Eq. (4), applying a very high bias field could render the transverse field noise negligible and remove the need for any transverse compensation at all, allowing for a reduction in complexity. As the technique is pushed to lower and lower operating frequencies, the method allows the measurement to evade the flicker noise $(1/f)$ of the detection electronics, by effectively mixing-up the low frequency ω_{RF} to the detected higher frequency ω_0, within the atomic medium. RF-AM systems that have tighter linewidths will be able to push lower in frequency as one-photon excitation by the coupling field will be attenuated and a few unshielded RF-AMs have already demonstrated linewidths on the order of tens of Hz.[7,19]

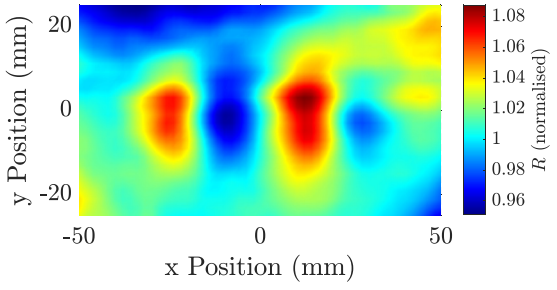

FIG. 6. Two-photon EMI imaging of the double-hole target concealed by a 3.2 mm thick Al skin. Here, $\omega_{RF}/2\pi = 410$ Hz with the resonant frequency set at $\omega_0/2\pi = 53$ kHz. For each pixel, the portable RF-AM is moved by a 2 mm step in the x–y plane and a Gaussian filter with a width of 1 pixel is used to smooth the image.

This work was funded by EPSRC Impact Acceleration Account (Grant No. EP/R511638/1).

AUTHOR DECLARATIONS

Conflict of Interest

The authors have no conflicts to disclose.

Author Contributions

Benjamin Maddox: Conceptualization (equal); Data curation (lead); Investigation (equal); Methodology (lead); Writing – original draft (lead). **Ferruccio Renzoni:** Conceptualization (equal); Funding acquisition (lead); Investigation (equal); Project administration (lead); Writing – review & editing (equal).

DATA AVAILABILITY

The data that support the findings of this study are available from the corresponding author upon reasonable request.

REFERENCES

[1]H. Griffiths, "Magnetic induction tomography," Meas. Sci. Technol. **12**, 1126 (2001).
[2]I. Savukov, S. Seltzer, and M. Romalis, "Detection of NMR signals with a radio-frequency atomic magnetometer," J. Magn. Resonance **185**, 214–220 (2007).
[3]C. Deans, L. Marmugi, S. Hussain, and F. Renzoni, "Electromagnetic induction imaging with a radio-frequency atomic magnetometer," Appl. Phys. Lett. **108**, 103503 (2016).
[4]A. Wickenbrock, N. Leefer, J. W. Blanchard, and D. Budker, "Eddy current imaging with an atomic radio-frequency magnetometer," Appl. Phys. Lett. **108**, 183507 (2016).
[5]P. Bevington, L. Wright, R. Gartman, and W. Chalupczak, "Role of the primary radio frequency magnetic field distribution in atomic magnetometer based inductive measurements," J. Appl. Phys. **131**, 164502 (2022).
[6]P. Bevington, R. Gartman, and W. Chalupczak, "Magnetic induction tomography of structural defects with alkali–metal spin maser," Appl. Opt. **59**, 2276–2282 (2020).
[7]L. Rushton, T. Pyragius, A. Meraki, L. Elson, and K. Jensen, "Unshielded portable optically pumped magnetometer for the remote detection of conductive objects using eddy current measurements," arXiv:2206.04631 (2022).
[8]W. Zheng, H. Wang, R. Schmieg, A. Oesterle, and E. S. Polzik, "Entanglement-enhanced magnetic induction tomography," arXiv:2209.01920v2 (2022).
[9]J. E. Dhombridge, N. R. Claussen, J. Iivanainen, and P. D. Schwindt, "High-sensitivity rf detection using an optically pumped comagnetometer based on natural-abundance rubidium with active ambient-field cancellation," Phys. Rev. Appl. **18**, 044052 (2022).
[10]C. Deans, L. Marmugi, and F. Renzoni, "Sub-picotesla widely tunable atomic magnetometer operating at room-temperature in unshielded environments," Rev. Sci. Instrum. **89**, 083111 (2018).
[11]H. Yao, B. Maddox, and F. Renzoni, "High-sensitivity operation of an unshielded single cell radio-frequency atomic magnetometer," Opt. Express **30**, 42015–42025 (2022).

[12]R. Zhang, Y. Ding, Y. Yang, Z. Zheng, J. Chen, X. Peng, T. Wu, and H. Guo, "Active magnetic-field stabilization with atomic magnetometer," Sensors **20**, 4241 (2020).
[13]X. Geng, G. Yang, P. Qi, W. Tang, S. Liang, G. Li, and G. Huang, "Laser-detected magnetic resonance induced by radio-frequency two-photon processes," Phys. Rev. A **103**, 053112 (2021).
[14]P. A. Bottomley and E. R. Andrew, "RF magnetic field penetration, phase shift and power dissipation in biological tissue: Implications for NMR imaging," Phys. Med. Biol. **23**, 630 (1978).
[15]C. Deans, Y. Cohen, H. Yao, B. Maddox, A. Vigilante, and F. Renzoni, "Electromagnetic induction imaging with a scanning radio frequency atomic magnetometer," Appl. Phys. Lett. **119**, 014001 (2021).
[16]B. Maddox, Y. Cohen, and F. Renzoni, "Through-skin pilot-hole detection and localization with a mechanically translatable atomic magnetometer," Appl. Phys. Lett. **120**, 014002 (2022).
[17]B. Maddox, Y. Cohen, and F. Renzoni, "Imaging corrosion under insulation with a mechanically-translatable atomic magnetometer," in *IEEE International Workshop on Metrology for Industry 4.0 & IoT (MetroInd4. 0&IoT)* (IEEE, 2022), pp. 104–108.
[18]P. Bevington, R. Gartman, and W. Chalupczak, "Inductive imaging of the concealed defects with radio-frequency atomic magnetometers," Appl. Sci. **10**, 6871 (2020).
[19]P. Bevington, R. Gartman, D. Botelho, R. Crawford, M. Packer, T. Fromhold, and W. Chalupczak, "Object surveillance with radio-frequency atomic magnetometers," Rev. Sci. Instrum. **91**, 055002 (2020).
[20]P. Bevington, R. Gartman, and W. Chalupczak, "Enhanced material defect imaging with a radio-frequency atomic magnetometer," J. Appl. Phys. **125**, 094503 (2019).
[21]J. D. Zipfel, S. Santosh, P. Bevington, and W. Chalupczak, "Object composition identification by measurement of local radio frequency magnetic fields with an atomic magnetometer," Appl. Sci. **12**, 8219 (2022).
[22]P. Bevington, R. Gartman, and W. Chalupczak, "Imaging of material defects with a radio-frequency atomic magnetometer," Rev. Sci. Instrum. **90**, 013103 (2019).